Supporting Information

Spin Polarization Assisted Facile C-H Activation by an *S* = 1 Iron(IV)-Bisimido Complex: A Comprehensive Spectroscopic and Theoretical Investigation

Jin Xiong,[a] Qing Liu,[b] Barbara Lavina,[c,d] Michael Y. Hu,[c] Jiyong Zhao,[c] Esen E. Alp,[c] Liang Deng,[b,*] Shengfa Ye,[e,*] Yisong Guo[a,*]

[a.] Department of Chemistry, Carnegie Mellon University, Pittsburgh, Pennsylvania, 15213, United States.
Email: ysguo@andrew.cmu.edu
[b.] State Key Laboratory of Organometallic Chemistry, Shanghai Institute of Organic Chemistry, Chinese Academy of Sciences, Shanghai, 200032, P. R. China.
Email: deng@sioc.ac.cn
[c.] Advanced Photon Source, Argonne National Laboratory, Argonne, Illinois, 60439, United States.
[d.] Center for Advanced Radiation Sources, University of Chicago, Chicago, Illinois, 60439, United States
[e.] State Key Laboratory of Catalysis, Dalian Institute of Chemical Physics, Chinese Academy of Sciences, Dalian 116023, P. R. China.
Email: shengfa.ye@dicp.ac.cn

Table of Contents

Synthesis

General Information: All manipulations on air- and moisture-sensitive materials were performed under an atmosphere of dry dinitrogen with the rigid exclusion of air and moisture using standard Schlenk or cannula techniques, or in a glovebox. Solvents were dried with a solvent purification system (Innovative Technology) and degassed prior to use. [(IPr)Fe(η^2:η^2-dvtms)],[1] 2-phenyl-2-azido-propane,[2] 1,1,1,3,3,3-hexaflouro-2-phenyl-2-azido-propane,[3] 2-azido-1,3-diisopropylbenzene,[4] and $^{57}FeCl_2$ [5] were synthesized according to literature procedures. All other chemicals were purchased from chemical vendors and used as received unless otherwise noted.

Preparation of [(IPr)^{57}Fe(NDipp)$_2$] (1). This complex was synthesized via similar procedures reported before[6]. To a stirred solution of [(IPr)Fe(η^2:η^2-dvtms)] (350 mg, 0.56 mmol) in toluene (5 mL) was added DippN$_3$ (225 mg, 1.12 mmol) at room temperature. The color of the solution changed from green to red immediately, and bubbles were released vigorously. The reaction system was kept stirring for 2 h at room temperature. The volatiles were then removed under a vacuum to leave a red residue. The red residue was extracted with Et_2O/THF (2:1, 12 mL) and the extraction was filtered. Standing the clear filtrate at room temperature to evaporate solvent afforded **1** as red crystals (312mg, 70%) suitable for single-crystal X-ray diffraction study.

Preparation of [(IPr)^{57}Fe(η2:η2-dvtms)]. This complex was synthesized according to the same synthetic procedures of [(IPr)Fe(η^2:η^2-dvtms)]. [6] To a stirring THF (50 mL) solution of IPr (630 mg, 1.00 mmol) were added $^{57}FeCl_2$ (128 mg, 1.00 mmol) and dvtms (190 mg, 1.02 mmol) at room temperature. KC_8 (280 mg, 2.10 mmol) was then added, and the

reaction system was kept stirring for 12 h at room temperature, during which the color changed to blue gradually. The mixture was then filtered through Celite. The filtrate was subjected to vacuum to remove all the volatiles, which left [(IPr)^{57}Fe(η^2:η^2-dvtms)] (495 mg, 0.79 mmol) as green solid.

Preparation of [(IPr)^{57}Fe(NC(CF$_3$)$_2$Ph)$_2$] (^{57}Fe-2). This complex was synthesized according to the same synthetic procedures of **2**.[7] To a test tube containing a clear diethyl ether (8 mL) solution of [(IPr)^{57}Fe(η^2:η^2-dvtms)] (320 mg, 0.51 mmol) was layered carefully with *n*-hexane (5 mL). Then a *n*-hexane (5 mL) solution of Ph(CF$_3$)$_2$CN$_3$ (288 mg, 1.03 mmol) was layered carefully on the top. The mixture was standing at -30 °C for 2 days, during the course olive-green crystals were formed on the tube wall. The green crystals were collected by filtration, washed with *n*-hexane (1 mL x 3) quickly, and then dried under vacuum, which leaves [(IPr)Fe(NC(CF$_3$)Ph$_2$)$_2$] (**1**) as a olive-green crystalline solid (280 mg, 60%).

Methods

X-ray crystallography: A qualified single crystal of complex **1** (with dimensions of 0.12×0.08×0.05 mm^3) and **2** (with dimensions of 0.08×0.05×0.04 mm^3) were mounted on the *Bruker D8 Venture* diffractometer equipped with a Ga source under N_2 atmosphere of 170 K. Data processing was accomplished with *SAINT v8.37A* (Bruker, 2015) software. SADABS method was utilized for absorption correction. The structures were solved by dual-space algorithm with *SHELXT 2015* [8] and refined on F^2 anisotropy for all the non-hydrogen atoms using the full-matrix least squares method using *SHELXL 2015* program[9]. Olex 2 UI[10] was applied in the solution and refinement. Details crystallographic data was listed in Table S1.

Physical measurements: Mössbauer spectra were collected with two spectrometers employing *Janis Research* (Wilmington, MA) *SuperVaritemp Dewars* equipped with a *LakeShore Model 331 A* temperature controller, which can perform in the temperature range from 1.5 to 240 K. One of the spectrometers is equipped with a permanent magnet that provides a constant magnetic field of 0.045 T. The other is equipped with a superconducting magnet that allows a field variation up to 8.0 T. The samples are prepared in a glove box by suspending well-ground polycrystalline powders into *Nujol* inside

polyoxymethylene cups and then freezing it soon with a cold Al block. *WMoss* software package (SEE Co, Edina, Minnesota) together with *SpinCount* software (Prof. Michael Hendrich, Carnegie Mellon University) are employed in the simulation. All the Mössbauer related figures are generated with *SpinCount* software. Isomer shifts are quoted relative to α-Fe foil standard at 298 K. Magnetic susceptibilities were measured from powder samples of solid material in the temperature range 2 - 300 K by using a SQUID susceptometer with a field of 0.1 T (MPMS-7, Quantum Design, calibrated with standard palladium reference sample, error <2%). Multiple-field variable-temperature magnetization measurements were done at 4 T, and 7 T also in the range 2- 300K with the magnetization equidistantly sampled on a 1/T temperature scale. The experimental data were corrected for underlying diamagnetism by use of tabulated Pascal's constants[11-12], as well as for temperature-independent paramagnetism. The susceptibility and magnetization data were simulated with our own package *julX*.

^{57}Fe Nuclear Resonant Vibrational Spectroscopy: The well-ground powder of each sample was suspended into *Nujol*, transferred into a special designed polyoxymethylene sample holder which has a *Kepton* tape window allowing X-ray to penetrate in. Then the whole cup was frozen with a cold Al block, and further stored in liquid nitrogen. The experiment was conducted at beamline 3ID at the Advanced Photon Source (APS), Argonne National Laboratory, IL, USA. The well-designed instrument equipped with a liquid helium cryostat and the sample was cooled with a copper cold finger. Samples were maintained at cryogenic temperatures in the liquid helium cryostat set to a temperature of approximately 20 K. The temperature for individual spectra were calculated using the ratio of anti-Stokes to Stokes intensity according to $S(-E) = S(E)\exp(-E/\mathrm{k}T)$ and were generally in the range of 40 K to 80 K. The monochromators provide a high energy resolution of ~ 1 meV by employing a water-cooled diamond (1,1,1) double crystal with 1.1 eV bandpass, followed by two separate Si(4,0,0) and Si(10,6,4) channel-cut crystals in a symmetric geometry. Single avalanche photodiode (APD) detector was used at both forward and perpendicular direction. A solid $K_2MgFe(CN)_6$ sample was used as energy calibration standard with a reference point of its Fe-C(ν7) vibrational mode reported at 74 meV.[13-14] The resolution function was collected by recording the delayed nuclear fluorescence at the forward direction simultaneously when the scattering photons were recorded at the

perpendicular direction. The spectra were recorded between -50 meV and +180 meV, 3 sec/step for each scan with a step size of 0.25 meV. Each scan required about 50 minutes, and all scans were added and normalized to the intensity of the incident beam. The program *PHEONIX-3.0.3*[15] was employed to process the data and derive the ^{57}Fe PVDOS.

Mössbauer simulation. The following spin Hamiltonian (Eq.1) was applied to describe the system. All the parameters are in their conventional meanings. To simulate ^{57}Fe Mössbauer spectra, all the terms were employed. The electron spin microstates and nuclear spin microstates can be easily decoupled under an external field larger than 10^2 Gauss because of the distinct magnitudes of Zeeman splitting. Therefore, we first solved the electron spin related terms with $|m_S>$ basis, then solved the other terms in the $|m_I>$ sub-space. The electron spin operator in the hyperfine term can be replaced by the expectation of electron spin (Eq. 2). Therefore, the calculation can be significantly simplified. The zero-field splitting (ZFS) term and quadrupole interaction term can be expanded as Eq.3&4, respectively. Notably, all the tensors do not necessarily have their frames aligned so we used different subscripts in Eq. 3&4. For dc magnetic data simulation, all the nuclear spin related terms were not included in the simulation.

$H = \beta_e \boldsymbol{B}\cdot\boldsymbol{g}\cdot\boldsymbol{S} + \boldsymbol{S}\cdot\boldsymbol{D}\cdot\boldsymbol{S} + \boldsymbol{S}\cdot\boldsymbol{A}\cdot\boldsymbol{I} - g_n\beta_n\boldsymbol{B}\cdot\boldsymbol{I} + \boldsymbol{I}\cdot\boldsymbol{Q}\cdot\boldsymbol{V}\cdot\boldsymbol{I})]$ (Eq. 1)

When $\beta_e \boldsymbol{B}\cdot\boldsymbol{g}\cdot\boldsymbol{S} \gg g_n\beta_n\boldsymbol{B}\cdot\boldsymbol{I}$, $\boldsymbol{S}\cdot\boldsymbol{A}\cdot\boldsymbol{I} = <\boldsymbol{S}>\cdot\boldsymbol{A}\cdot\boldsymbol{I}$ (Eq.2)

$$\boldsymbol{S}\cdot\boldsymbol{D}\cdot\boldsymbol{S} = D\left[(S_{z'}^{\mathbf{2}} - S(S+1)/3) + \frac{E}{D}\left(S_{x'}{}^2 - S_{y'}{}^2\right)\right] \quad , \quad D = \frac{3}{2}D_{z'z'} \quad , \quad E = \frac{D_{x'x'} - D_{y'y'}}{2}$$

where $|D_{z'z'}| > |D_{y'y'}| > |D_{x'x'}|$ (Eq. 3)

$$\boldsymbol{I}\cdot\boldsymbol{Q}\cdot\boldsymbol{V}\cdot\boldsymbol{I} = \frac{eQV_{z''z''}}{4I(2I-1)}[3I_{z''}{}^2 - I(I+1) + \eta\left(I_{x''}{}^2 - I_{y''}{}^2\right)], \eta = \frac{V_{x''x''} - V_{y''y''}}{V_{z''z''}}$$ (Eq. 4)

For the effective S = ½ spin Hamiltonian used to simulate the VTVH Mössbauer spectra of complex **2**, it has the following Hamiltonian matrix with $m_s = \pm 1/2$ as the basis (assuming $g_{\mathrm{eff,x}} = g_{\mathrm{eff,y}} = 0$):

$$\begin{bmatrix} \frac{1}{2}g_{\mathrm{eff,z}}\beta B & \frac{\Delta}{2} \\ \frac{\Delta}{2} & -\frac{1}{2}g_{\mathrm{eff,z}}\beta B \end{bmatrix}$$

By solving this Hamiltonian matrix, we obtain the energies of the effective spin sublevels to be $\varepsilon_{\pm} = \pm\frac{1}{2}\sqrt{{g_{\mathrm{eff,z}}}^2\beta^2B^2 + \Delta^2}$, and the corresponding wavefunctions of the sublevels to be $\phi_+ = \cos\alpha|1/2> + \sin\alpha|-1/2>$, and $\phi_- = \sin\alpha|1/2> - \cos\alpha|-1/2>$ where $\tan\alpha = \Delta/g_{\mathrm{eff,z}}\beta B$. The comparison of energy diagram for this solution and from an $S = 1$ spin Hamiltonian is shown in Figure S6. Using this solution, we can obtain the magnetization curve for the internal field ($B_{int} = -< S_{\mathrm{eff,z}} > A_{\mathrm{eff,z}}/g_n\beta_n$) as a function of B_{ext} (the externally applied field) (Figure S7) and as a function of temperature under a constantly applied external field (Figure S7). The magnetic behavior reflected by this effective $S = ½$ spin Hamiltonian can be well reproduced by the $|\pm1'>$ doublet of a canonical $S = 1$ spin Hamiltonian assuming the external field is applied along the z direction defined by the zero-field splitting tensor of the $S = 1$ Hamiltonian (Figure S7).

CASSCF/NEVPT2 calculations: To build the fragments, we truncated the dipp groups to phenyl groups, and then optimized all the H atoms coordinates but left all the non-H atoms fixed. Then CASSCF/NEVPT2 calculations were carried out with ORCA-5.0.3 release[16]. The Fe was described by def2-TZVPP basis set, while all the other atoms were described by def2-TZVP basis set.[17-18] The def2/JK auxiliary basis set was applied for the RIJK-approximation[19] to speed up the CASSCF calculations. The guess orbitals were generated based on localized quasi-restricted orbitals (QROs) generated by UKS calculations. Strongly contracted NEVPT2 (SC-NEVPT2) corrections were also applied to capture dynamic correlation effects. Quasi-degenerate perturbation theory (QDPT) calculations were used to calculate the spin-orbit coupling (SOC) related properties. ZFS related properties were computed with state-average CASSCF/NEVPT2 calculations (1 quintet root + 1 triplet root + 10 singlet roots for Complex **1&3**; 1 quintet root + 6 triplet roots + 1 singlet root for Complex **2**). The ground state CASSCF orbitals, spin density as well as EFG tensors shown in Figures 4-5&S10-S11 were computed with single root CASSCF/NEVPT2 calculations which only includes the ground state wavefunction (1 singlet root for Complex **1**&**3**, 1 triplet root for Complex **2**).

DFT calculations:

General method: Unless specified, the present DFT calculations were carried out using Gaussian 16 Rev C01[20]. BP86 functional[21-22] together were employed. All the atoms were described by TZVP basis set[23-24]. Optimization threshold was set to tight.

^{57}Fe PVDOS calculation: The crystal structure of each complex was optimized with DFT method. Optimization threshold was set to tight. Frequency analysis was followed by optimization to generate normal modes of vibration and their associated frequencies. The ^{57}Fe PVDOS was generated by using an in-house program that extracts the Cartesian normal mode displacements obtained by DFT frequency calculations and converts them into ^{57}Fe mode composition factor $e^2_{Fe,\alpha}$ based on the following equation[25]:

$$e^2_{Fe,\alpha} = \frac{m_{Fe} r^2_{Fe,\alpha}}{\sum_{\alpha} m_i r^2_{i,\alpha}} \qquad \text{(Eq. 5)}$$

where m_i and $r^2_{i,\alpha}$ are the mass of atom i and its mean square motion in mode α. The obtained ^{57}Fe mode composition factor was further used to reconstruct ^{57}Fe PVDOS spectra to compare with experimental data according to the following equation[25]:

$$D_{Fe}(\bar{\nu}) = \sum_{\alpha} e^2_{Fe,\alpha} \ell(\bar{\nu} - \bar{\nu}_{\alpha}) \qquad \text{(Eq. 6)}$$

where the line shape function $\ell(\bar{\nu} - \bar{\nu}_{\alpha})$ was generated by using a 10 cm^{-1} gaussian broadening to mimic the experimental energy resolution.

^{57}Fe isomer shift calculation: A reported calibration was employed to correlated ^{57}Fe isomer shift values and DFT-calculated electron density on Fe nucleus of complexes **1**-**3**.[26] Starting with crystal structures, the geometries were optimized with BP86 functionals and TZVP basis set using Gaussian 16 Rev c01. Then the total electron density on Fe nucleus, ρ(0), was generated with TPSSh functionals using ORCA-5.0.3. TZVP basis set was employed to describe all the atoms except Fe, which was described with CP(PPP) basis set. The results are listed in Table S5.

Geometric scan: Besides the general settings, a Grimm's D3 dispersion energy correction[27] was employed in the geometric scan. The following structural factors were

selected as investigation candidates: Fe-C/N bond lengths, N2=Fe1=N3 bond angle, Fe=N-C(R) bond angle, angle between NHC plane (defined by the 5-member ring) and FeN_2C plane and the C19-N2…N3-C23 dihedral angle. The crystal structure of Complex **2** was chosen as the starting point by truncating all the substituents of NHC and imido to methyl groups (so-called Me_Me in the main text) or other groups (like Me_CF_3 in the CN…NC dihedral angle scan, etc). A relaxed potential energy surface scan was carried out by varying the selected candidate while freezing all the other structural factors. For the angle between NHC plane and FeN2C plane, the dihedral angles N(NHC)-C(NHC)-Fe=N(imido) are selected as the factors to freeze or relax. We froze four of them when scanning other factor, but scan one of them to relax the angle between two planes. The two Fe-N bond lengths as are different, so we fixed their difference by varying them simultaneously with same step size. The same strategy was used for the Fe=N-C bond angles. In Figure S12-B&S13-B, the x-axis is generated by averaging the two bond lengths or angles. Notably, when the Fe=N-C angle is larger than 150º, the CN…NC dihedral angle fixation is less meaningful. Especially when the bond angle is close to linear, varying the CN…NC dihedral angle a lot would only lead to a small geometric change. Applying the corresponding restriction lead the program fail to find the next step, so we relax this dihedral angle. Anyway, the results still suggest that the singlet favors an almost linear Fe=N-C angle, while the triplet favors a bend angle around 140~145º.

Substituent-varying Geometric Optimization: The Grimm's D3 dispersion energy correction was also applied in the substituent-varying geometric optimization. The starting point for each geometry was built by replacing the substituents based on the crystal structure of either Complex **1**&**3**(for singlet) and Complex **2**(for triplet) during which process, the chemical intuition was also employed. The xyz coordinates of optimized geometries can be found in a separate SI file.

Thermodynamics: The CPCM polarizable conductor calculation model[28-29] of benzene solvent was employed in the calculations (both optimization and frequency analysis). 1,6-diisopropylbenzene (DippH) was selected as the substrate to mimic the intra-molecular reaction. The tertiary C-H bond in isopropyl group was selected for the targeting C-H bond because the corresponding radical is more stable. The starting geometries of all Fe-

containing species were built from crystal structures. For the protonated species, the proton of starting geometry was added in the help of chemical intuition. The optimization was done in different spin state, and the ones with lower free energy were selected. The xyz coordinates of optimized geometries can be found in a separate SI file. The calculated Gibbs free energies can be found in Tables S6&S7.

Comments on the mode assignments of ^{57}Fe PVDOS features. We provide some more analysis of the NRVS data from complexes **1** and **2** in the energy range lower than 800 cm^{-1}. The NRVS derived ^{57}Fe PVDOS spectra of complexes **1** and **2** are shown in Figure 2, which are compared with the DFT calculated spectra in the same figure. The major ^{57}Fe PVDOS features of complexes **1** and **2** can be understood by comparing the normal modes of vibrations of a simplified $MX(Y_2)_2$-type molecule. The full set of normal modes are shown in Figure S4. For complex **1**, the strongest PVDOS feature at 388 cm^{-1} is originated from the C(NHC)-Fe=NR bending motion (δ(C-Fe=NR)) and the RN=Fe=NR bending motion (δ(RN=Fe=NR)) mixed with Fe-C(NHC) stretching mode (ν(Fe-C)) (Figure 2). These two modes are predicted at 395 and 389 cm^{-1} by DFT. Between 150 and 200 cm^{-1}, the PVDOS features can be assigned to the Fe out of plane bending mode (π_{op}(Fe)). in mid-energy range (400 – 800 cm^{-1}), a feature located at 733 cm^{-1} most likely belongs to the symmetric Fe=N-R bending mode, which is predicted at 735 cm^{-1} by DFT. Due to the elongation of all the iron-ligand bonds in going from **1** to **2**, all the vibrational modes identified in complex 1 are shifted to lower frequencies as shown in Figure 2.

Comments on the analysis of dc magnetic measurements of 2. To probe the electronic structure of complex **2**, variable-temperature (VT) magnetic susceptibility and variable temperature variable-field (VTVH) magnetization measurements using superconducting quantum interference device were performed (Figure S9). The effective magnetic moment (μ_{eff}) of ~3.1 μ_B measured at 300 K and under 1 T external magnetic field is greater than the spin-only value for triplet systems (2.832 μ_B); therefore, complex **2** features an $S = 1$ ground state albeit with a sizeable unquenched orbital angular momentum. Remarkably, as the temperature decreases, μ_{eff} first reaches a maximum at ~70 K, which reflects the very large g anisotropy of the system. As a consequence of distinct $g_{\parallel}$ and $g_{\perp}$ factors, the magnetic moment of the lowest-energy magnetic sublevels that are preferentially populated

at cryogenic temperatures can substantially surpass the average magnetic moment of the entire spin manifold that are equally populated at room temperature. Then, μ_{eff} drops precipitately below 50 K, which primarily arises from the strong magnetic anisotropy of complex **2**, consistent with the nesting isofield curves observed for the VTVH magnetization measurements. Over the course of simultaneous fit of both sets of the data with a usual $S = 1$ spin Hamiltonian, we found that the system has a large negative D value, but because D and g are strongly correlated, precise values of these spin Hamiltonian parameters cannot be determined. Figure S9 presents a reasonable fit, for which D was fixed to be –79 cm^{-1}, the value estimated by CASSCF/NEVPT2 calculations (see below), with the following parameters: E/D = 0.085 (the same value used for the Mössbauer simulations), $g_{\perp} = 1.83$, $g_{\parallel} = 2.80$, TIP = 1188 × 10^{-6} emu (TIP = temperature-independent paramagnetism). Of note, TIP results from mixing of the ground and excited states induced by the applied magnetic field, so called the second-order Zeeman effect. Thus, the large TIP and D values both suggest that there exist low-lying excited states in complex **2** as exemplified by $S = 1$ ferrous tetraphenylporphyrin.[30]

Comments on the DFT-based thermodynamic analysis. To analyze the thermodynamic driving force of the HAT step by the Fe(IV)-bisimido complexes and connect this with the reduction potentials and the basicity of these complexes, we adopted a thermodynamic analysis proposed by Srnec and coworkers.[31] Based on the classical thermodynamic box scheme of the bond dissociation free energy (BDFE) of a N-H bond in an Fe(III)-amide complex (Figure S15), the BDFE can also be estimated by the free energies of two sequential steps: 1) a protonation (or proton transfer, PT) to an Fe(IV)-bisimido complex ($pK_{\text{a,ox}}$) followed by a reduction (or electron transfer, ET) of the protonated Fe(IV)-bisimido complex to an Fe(III)-amide complex (E^{0}'), or 2) a reduction of the Fe(IV)-bisimido complex to an Fe(III)-bisimido complex (E^{0}) followed by a protonation to this Fe(III)-bisimido complex to form the same Fe(III)-amide complex ($pK_{\text{a,red}}$). Srnec and coworkers defined an effective reduction potential $E^{0}_{\text{eff}} = \frac{1}{2}(E^{0}' + E^{0})$ and an effective basicity $pK_{\text{a,eff}} = \frac{1}{2}(pK_{\text{a,ox}} + pK_{\text{a,red}})$ to describe these two thermodynamic variables. Then the BDFE of a N-H bond in an Fe(III)-amide complex can be expressed as:

$$E^{0}{}_{H} = E^{0}{}_{\text{eff}} + \frac{RT}{F} \times \ln(10) \times pK_{a,\text{eff}} \quad \text{(Eq. 7)}$$

where E^0_H has the unit of milli-volts (mV) and $(RT/F) \times \ln(10) = 0.0591$ V at 298 K. A similar treatment can be applied to the BDFE of a C-H bond in a substrate (Figure S16) and expressed as:

$$E^{0,\text{sub}}{}_H = E^{0,\text{sub}}{}_{\text{eff}} + \frac{RT}{F} \times \ln(10) \times pK_{a,\text{eff}}{}^{\text{sub}} \quad \text{(Eq. 8)}$$

Then, the overall thermodynamic driving force for the HAT step can be expressed as

$$\Delta G^0{}_{\text{HAT}} = -F \times \Delta E^0{}_H = -F \times \Delta E^0{}_{\text{eff}} - RT \times \ln(10) \times \Delta pK_{a,\text{eff}} \quad \text{(Eq. 9)}$$

where $\Delta E^0_H = E^0_H - E^{0,\text{sub}}_H$, $\Delta E^0_{\text{eff}} = E^0_{\text{eff}} - E^{0,\text{sub}}_{\text{eff}}$, and $\Delta pK_{a,\text{eff}} = pK_{a,\text{eff}} - pK_{a,\text{eff}}{}^{\text{sub}}$. In this way, a correlation plot between ΔE^0_{eff} and $\Delta pK_{a,\text{eff}}$ can be constructed, and the projection of any point on this plot to the diagonal ΔE^0_H axis represent the thermodynamic driving force of the HAT step (Figure S17).

By following this analysis, we calculated the HAT driving forces of complex **1** – **3** and plotted onto the ΔE^0_{eff} vs. $\Delta pK_{a,\text{eff}}$ plot (Figure S13 and Tables S3 – S5). The results suggest that the overall HAT process by using the tertiary C-H bond of DippH as the substrate is endergonic under room temperature (298 K) for all three complexes with complex **2** involved in the least endergonic reaction ($\Delta G^0_{\text{HAT}} = 5.9$ kcal/mol, Table S5). For complex 1 and 3, $\Delta G^0_{\text{HAT}} = 13.9$ kcal/mol and 16.1 kcal/mol. The ΔG^0_{HAT} estimated in our analysis for the reaction involving **2** compares well with ΔG^0_{HAT} obtained previously in the reaction coordinate calculations ($\Delta G^0_{\text{HAT}} = 6.9$ kcal/mol). $\Delta pK_{a,\text{eff}}$ for complex **1** and **3** are 470 and 644 mV (converting to mV by multiply $\Delta pK_{a,\text{eff}}$ by 0.059 V) respectively and are higher than $\Delta pK_{a,\text{eff}}$ of complex 2 (204 mV), which suggest that complex **2** has a reduced basicity due to the use of the electron-withdrawing substituent than those of complexes **1** and **3**. However, this drawback is overcome by the significant increase in ΔE^0_{eff} of **2** (-462 mV) for more than 600 mV than those of **1** (-1075 mV) and **3** (-1344 mV). Therefore, we conclude that the higher reduction potential of complex **2** is likely the dominant factor to demonstrate more facile HAT reactivity than complexes **1** and **3**, thus rendering **2** being more reactive than the $S = 0$ complexes.

Supplementary tables

Table S1. Crystallographic data and structure refinements of Compound **1** and **2**.

Complex	1	2
Formula	$C_{51}H_{70}FeN_4$	$C_{45}H_{46}F_{12}FeN_4$
Formula weight	794.96	926.71
Crystal system	Monoclinic	Monoclinic
Space group	*C* 2/c	*P* 2_1/n
***a*, Å**	23.1585(7)	11.1466(5)
***b*, Å**	9.2604(3)	18.2778(8)
***c*, Å**	23.5718(7)	21.1859(9)
***β*,°**	114.448(2)	91.163(2)
***V*, Å^3**	4601.9(3)	4315.4(3)
Z	4	4
***T*, K**	170	170
F(000)	1720.0	1912.0
***λ*, Å**	1.34139	1.34139
Data completeness	0.985	0.993
R1	4.30%	4.56%
wR2 (all data)	12.22%	11.16%
S	1.093	1.035
Bond precision (C-C) , Å	0.0040	0.0038

Table S2. Comparison of selected structural parameters between x-ray crystallography (Exp) under 170 K and DFT optimization (calc, BP86/TZVP/GD3) results for complex **1**-**3**, as well as various truncated models. Bond lengths are in angstrom (Å), angles are all in degree (°), and energies are in kcal/mol.

Fragment	Fe-C	Fe-N^{imido}	N^{imido}-C	CN … NC	C-N=Fe	N-C-Fe-N	N=Fe=N	Δ*E*
1 (Exp)	1.916	1.638	1.376	-25	173	35, -145, -145, 35	143	-
2 (Exp)	2.049	1.705,1.712	1.438,1.435	-70	144, 141	78, -106, -93, 84	125	-

3 (Exp)	1.928	1.614,1.617	1.455,1.440	1	161, 160	-6, 175, 176, -3	128	-
1 (Calc, S)	1.858	1.649	1.356	-23	173	34, -146, -146, 34	151	0
1 (Calc, T)	1.915	1.712,1.710	1.353,1.362	-96	159, 144	22, -164, -158, 16	144	11.47
2 (Calc, S)	1.923	1.642,1.622	1.429,1.417	-26	146, 165	107, -75, -80, 99	131	0
2 (Calc, T)	1.994	1.692,1.661	1.441,1.421	-69	133, 153	-107, 91, 82, -79	124	-0.44
3 (Calc, S)	1.893	1.620,1.619	1.444,1.442	-8	161, 160	10, -165, -168, 17	132	0
3 (Calc, T)	1.993	1.681,1.658	1.456,1.435	-61	134, 153	-101, 96, 87, -76	123	14.84
Me_Me (S)	1.877	1.622	1.418	0	168	2, 178, -178, -2	139	0
Me_Me (T)	1.959	1.676,1.674	1.437,1.429	-85	135, 142	5, -159, -177, 19	127	10.10
Me_1-Ad (S)	1.883	1.630,1.634	1.431,1.430	-10	146	18, 178, -162, -2	134	0.00
Me_1-Ad (T)	1.958	1.663,1.681	1.432,1.435	-80	140, 138	29, 177, -144, 5	124	8.63
Me_2-Ad (S)	1.887	1.631,1.634	1.422,1.429	-16	152, 145	18, -144, 161, 37	135	0
Me_2-Ad (T)	1.962	1.678,1.666	1.428,1.431	-71	145, 138	17, -130, -174, 39	123	8.15
Me_CF_3 (S)	1.884	1.638,1.644	1.387,1.386	-15	153, 154	45, -151, -133, 31	147	0
Me_CF_3 (T)	1.948	1.695,1.691	1.390,1.382	-122	128, 139	23, -150, -157, 30	136	1.02
Me_Cyh (S)	1.888	1.628,1.630	1.430,1.428	1	151, 149	1, 165, 179, -17	134	0
Me_Cyh (T)	1.965	1.678,1.668	1.438,1.434	-76	138, 140	4, -150, 179, 25	124	8.17
Me_Dipp (S)	1.876	1.645,1.643	1.356,1.357	10	169, 167	-19, 152, 163, -26	147	0
Me_Dipp (T)	1.979	1.693,1.677	1.364,1.362	-55	143, 146	3, -152, -180, 25	121	7.06
Me_tBu (S)	1.885	1.629,1.625	1.443,1.444	8	149, 150	3, 165, -178, -15	134	0
Me_tBu (T)	1.958	1.677,1.672	1.452,1.445	-84	140, 134	4, -159, -179, 19	126	7.99
Me_Ph (S)	1.880	1.647	1.363	-1	153	10, 171, -170, -9	142	0
Me_Ph_T	1.919	1.682,1.683	1.367,1.359	-24	139, 143	35, 168, -135, -1.4	124	0.30
Me_RF_S	1.886	1.642	1.398,1.399	-5	169, 167	84, -90, -97, 89	163	0
Me_RF (T)	1.952	1.691,1.690	1.423,1.410	-110	134, 142	21, -149, -159, 31	135	2.79
Me_Ms (S)	1.891	1.644,1.652	1.720,1.710	-23	132, 136	33, 180, -140, 6	135	0
Me_Ms (T)	1.930	1.680,1.673	1.689,1.697	-12	133, 134	-3, -138, 170, 35	121	-4.88
Me_Vn (S)	1.882	1.641	1.348,1.349	5	172, 170	24, -158, -157, 21	142	0
Me_Vn (T)	1.966	1.698	1.356	-89	140	-7, 173, 173, -7	130	7.22

Me_H (S)	1.881	1.628	1.030	0	147	9, 172, -172, -9	139	0
Me_H (T)	1.931	1.682	1.037	0	128	6, 174, -174, -6	133	3.87
1-Ad_1-Ad (S)	1.942	1.628,1.634	1.417,1.418	14	169, 166	-84, 101, 95, -80	145	0
1-Ad_1-Ad (T)	2.031	1.669,1.676	1.435,1.432	-77	140, 136	-96, 69, 82, -113	121	2.30
2-Ad_2-Ad (S)	1.889	1.637	1.414	93	166	-50, 130, 129, -51	151	0
2-Ad_2-Ad (T)	1.975	1.682,1.663	1.437,1.433	-72	135, 139	29, -118, -168, 45	120	10.46
CF_3_CF_3 (S)	1.876	1.633,1.634	1.396,1.397	-19	155, 158	46, -146, -132, 36	144	0
CF_3_CF_3 (T)	1.958	1.676,1.682	1.399,1.393	-97	130, 139	-26, 169, 151, -15	127	1.58

*CN…NC refers to the C19-N2…N3-C23 dihedral angle, N-C-Fe-N refers to the four N(NHC)-C(NHC)-Fe-N(imido) dihedral angles, Δ*E* refers to the energy referring to corresponding singlet state species.
**Nomenclature: X_Y (S/T), X represents the substituents on HNC ring, Y represents the substituent on imido, S, T represents the singlet or the triplet state, respectively.
***Optimization was carried out with C1 point group, but some optimized structures are very close to C2 symmetry.
**** 1-Ad = 1-admantyl, 2-Ad = 2-admantyl, tBu = tert-butyl, Cyh = cyclohexyl, Dipp = di-isopropylphenyl, Ms = SO_2Me, RF = $C(CF_3)_3$, Vn = vinyl, Ph = phenyl.

Table S3. Summary of iron-imido vibration assignments and comparisons. [a]

Complex	*d*(Fe=NR)	π_{op}(Fe)	δ(RN=Fe=NR)+ ν(Fe-C)	δ(C-Fe=NR)	δ(Fe=N-R)	ν(Fe=NR)	ν_{as}(N-R)	Ref [b]
1	1.638	170 (*169*), 185 (*191*), 205 (207)	376 (*389*)	388 (*395*)	733 (*735*) s	968 (*968*) s 988 (*995*) as	1285, 1322 (*1302*, *1350*) as	This work
2	1.709	133 (*148*), 162 (*184*), 180 (*199*)	332 (*346*)	316 (*336*)	543 (*545*, *539*, *533*)	814 (*826*) s 858 (*861*) as	1139, 1173 (*1060*, *1070*, *1155*, *1180*)	This work
$[Fe^{IV}(NTs)(MePy_2tacn)]^{2+}$	1.71	-	-	-	-	984	-	Ref 38
$[Fe^{IV}(NTs)(Me_2CHPy_2tacn)]^{2+}$	1.72	-	-	-	-	1061	-	Ref 38
$[Fe^{IV}(NTs)(N4py)]^{2+}$	1.73	-	-	-	-	998	-	Ref 35
$[(TAML)Fe^{V}(NTs)]^{-}$	1.65	-	-	-	-	817	-	Ref 34
$[PhBP_3]Fe^{III}N^tBu$	1.635	-	-	-	-	1104	1233	Ref 75
$[PhBP_3]Fe^{III}N$(1-Ad)	1.641	-	-	-	-	1097	1225	Ref 75

$[PhBP_3]Fe^{III}NPh$	-	-	-	-	-	958	1292/1309	Ref 75
$[PhBP_3]Fe^{III}N(p\text{-tolyl})$	1.659	-	-	-	-	962	1281/1305	Ref 75
$[Fe_4(\mu_3\text{-}N^tBu)_4(N^tBu)Cl_3]$	1.635	-	-	-	-	1111	1214	Ref 75

[a] The italic numbers are derived from DFT calculations. Distances are in Å, and vibrational frequencies are in cm^{-1}. [b] References quoted in the main text.

Table S4. NEVPT2 corrected low-lying states energies of complex **1**-**3**.

Complex 1		**Complex 2**		**Complex 3**	
Multiplet	***E*** **(cm^{-1})**	**Multiplet**	***E*** **(cm^{-1})**	**Multiplet**	***E*** **(cm^{-1})**
S	0	T	0	S	0
T	4400.2	T	1021.8	T	4416.6
S	9628.8	Q	2796.2	Q	8336.5
S	9944.9	S	2999.3	S	11849.4
Q	10038.9	T	7455.8	S	11955.3
S	10926.0	T	8321.6	S	13178.6
S	14900.2	T	8457.1	S	14856.0
S	17207.1	T	11004.5	S	16391.8
S	17788.0			S	20000.0
S	24532.5			S	26651.9
S	24859.7			S	26740.0
S	25762.8			S	26835.3

Table S5. Mössbauer parameters derived from experimental data or calculations.

Complex (Method)	δ(mm/s)	ΔE_Q(mm/s)	η
1 (Exp)	-0.28	-1.84	0.4
1 (DFT)	-0.419	-2.711	0.63
1 (CASSCF)	-	-1.744	0.49
2 (Exp)	-0.10	-1.02	Not determined
2 (DFT)	-0.191	-1.756	0.81
2 (CASSCF)	-	-1.905	0.39
3 (Exp)	-0.41	2.40 [a]	0
3 (DFT)	-0.526	+3.189	0.98
3 (CASSCF)	-	-1.813	0.94

[a] The sign is not determined.

Table S6. DFT calculated Gibbs free energy (E+ZVE+Gibbs correction in a.u.) of each key Fe species.

	$^3Fe^{IV}$	$^1Fe^{IV}$	$^3Fe^{IV}$_NH	$^1Fe^{IV}$_NH	$^4Fe^{III}$	$^2Fe^{III}$	$^4Fe^{III}$_NH	$^2Fe^{III}$_NH
1	-3468.2363	-3468.2439	-3468.6811	-3468.6661	-3468.3266	-3468.3301	-3468.8485	-3468.8370
2	-4423.9166	-4423.9152	-4424.3358	-4424.3221	-4424.0140	-4424.0171	-4424.5340	-4424.5266
3	-3232.4215	-3232.4306	-3232.8709	-3232.8616	-3232.4899	-3232.5036	-3233.0318	-3233.0299

*Fe^{IV} = $[LFe^{IV}(NR)_2]$, Fe^{IV}_NH = $[LFe^{IV}(HNR)(NR)]^+$, Fe^{III} = $[LFe^{III}(NR)_2]^-$, Fe^{III}_NH = $[LFe^{III}(HNR)(NR)]$.

Table S7. DFT calculated Gibbs free energy (E+ZVE+Gibbs correction in a.u., 298.15 K) of each key substrate related species.

Species	RH	$^2[RH]^+$	$^2R^-$(anion)	$^2R^{\cdot}$(radical)
DippH*	-468.0482	-467.7865	-467.4922	-467.4213

*the tertiary C-H in the isopropyl group.

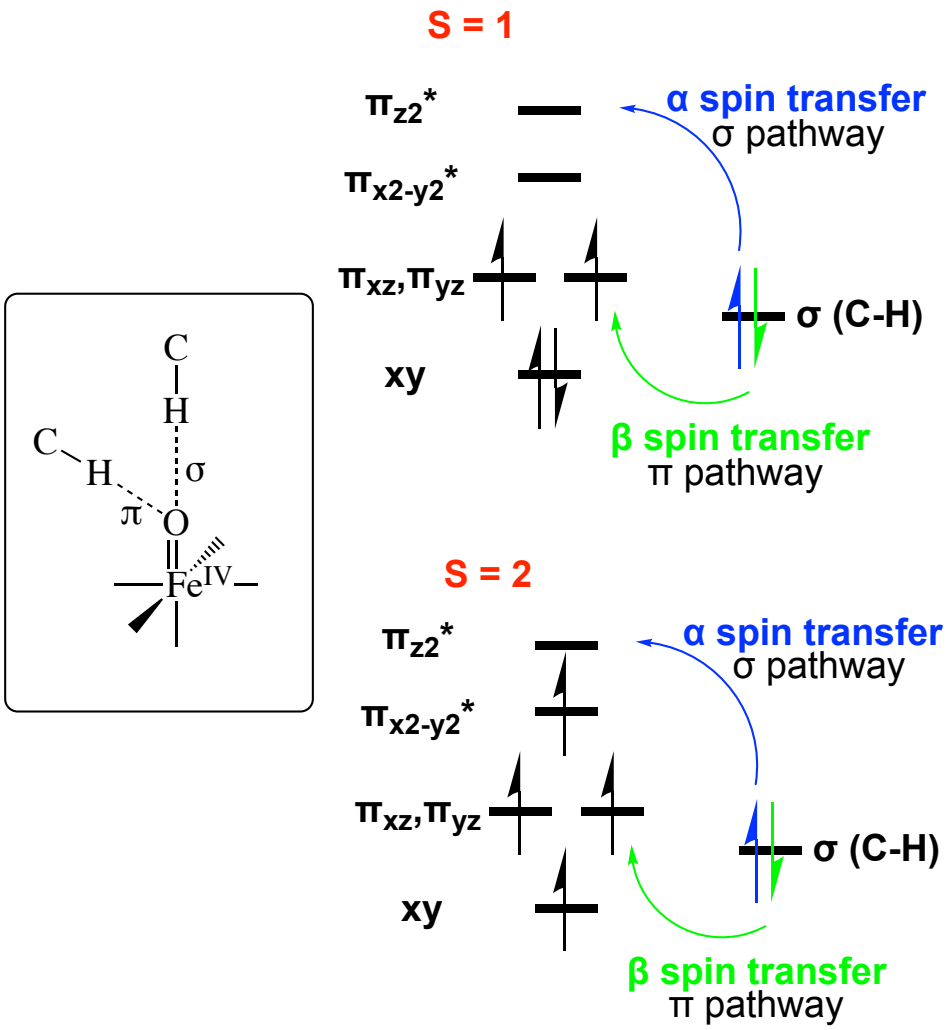

Scheme 1. Electron transfer pathways and the two possible substrate approaching trajectories for the HAT processes in the well-studied Fe(IV)-oxido species in both triplet and quintet spin state.

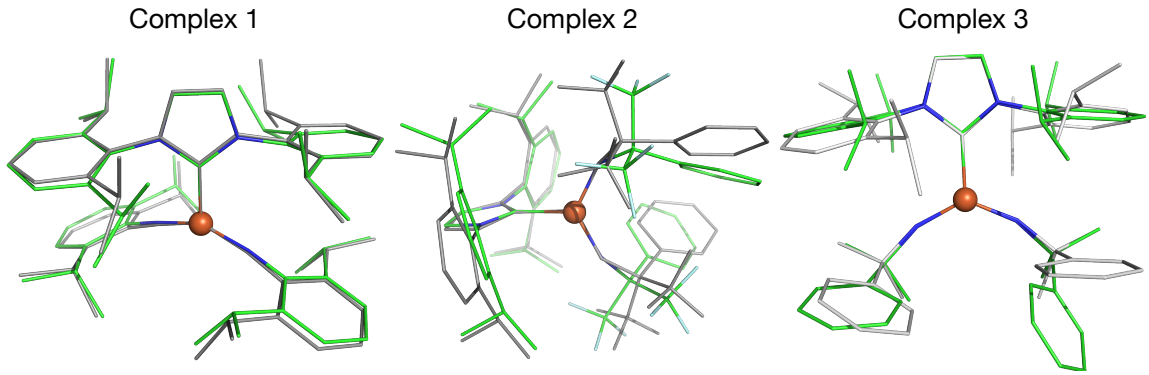

Figure S1. Structural overlays of the crystal structures and the DFT optimized structures of complexes **1**-**3**. The structures in grey are the crystal structures and the structures in color are the DFT optimized ones. The DFT method: BP86/TZVP with GD3 correction.

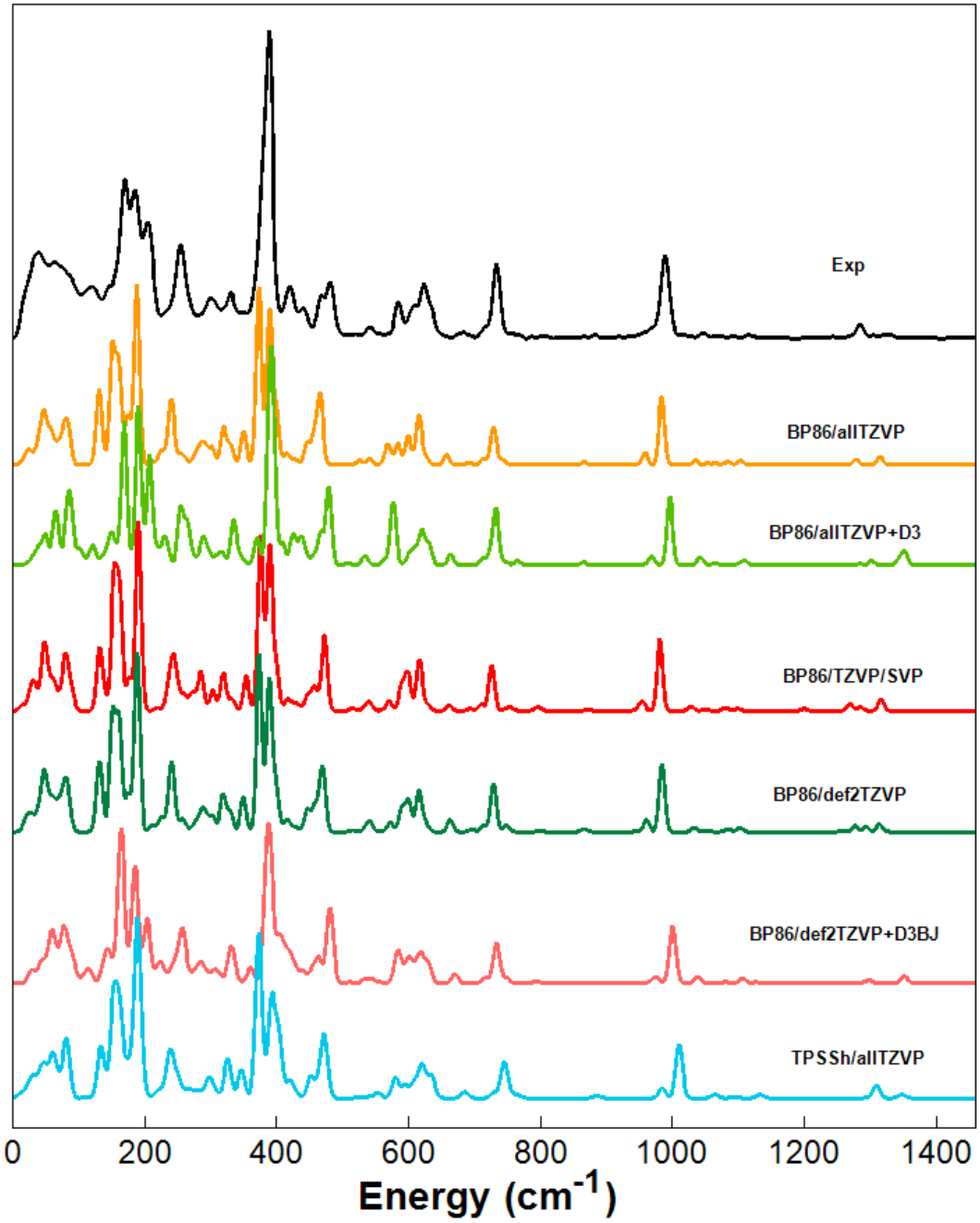

Figure S2. Comparison among NRVS derived and calculated PVDOS employing indicated functionals and basis set combinations for Complex **1**.

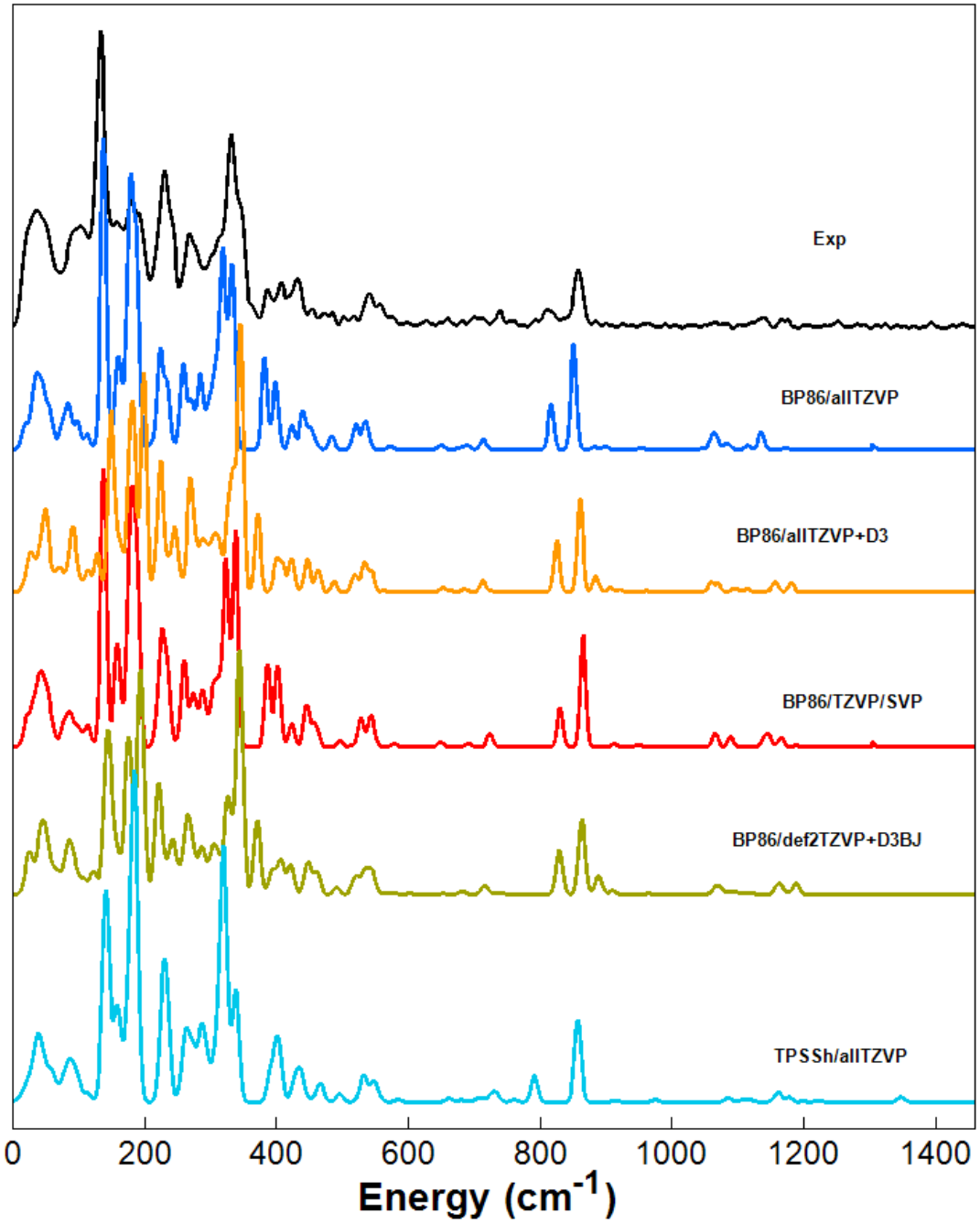

Figure S3. Comparison among NRVS derived and calculated PVDOS employing indicated functionals and basis set combinations for Complex **2**.

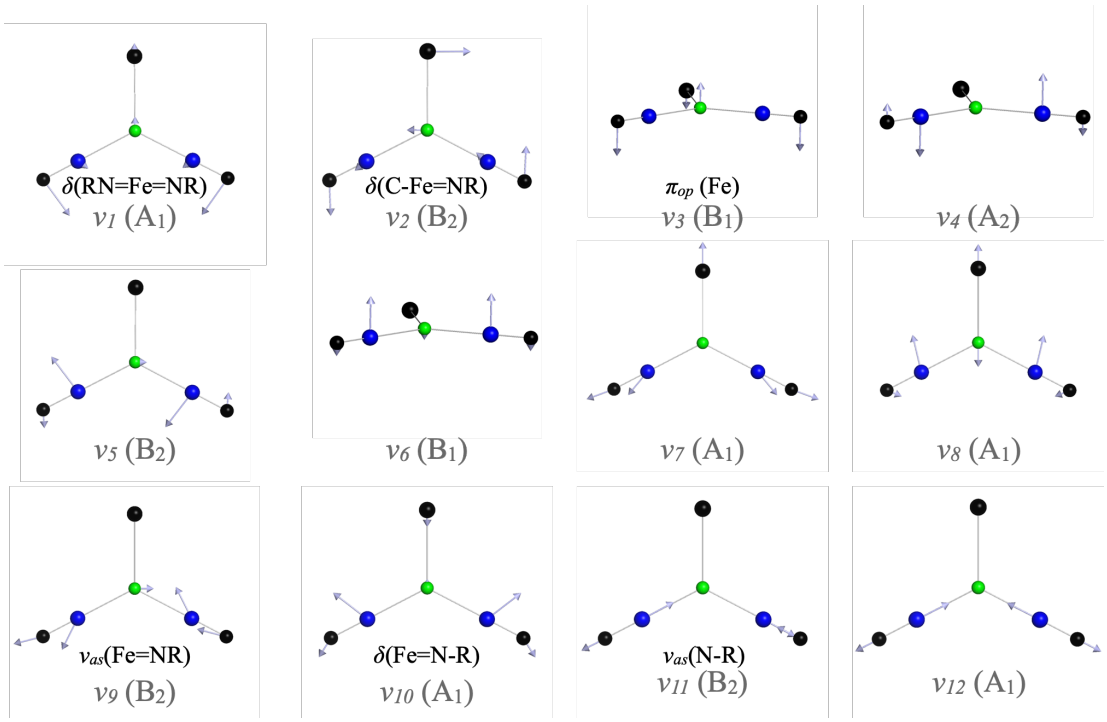

Figure S4. Normal modes of vibration derived from $MX(Y_2)_2$ model. The selected modes that is assigned to the ^{57}Fe PVDOS features shown in Figure 2 are indicated.

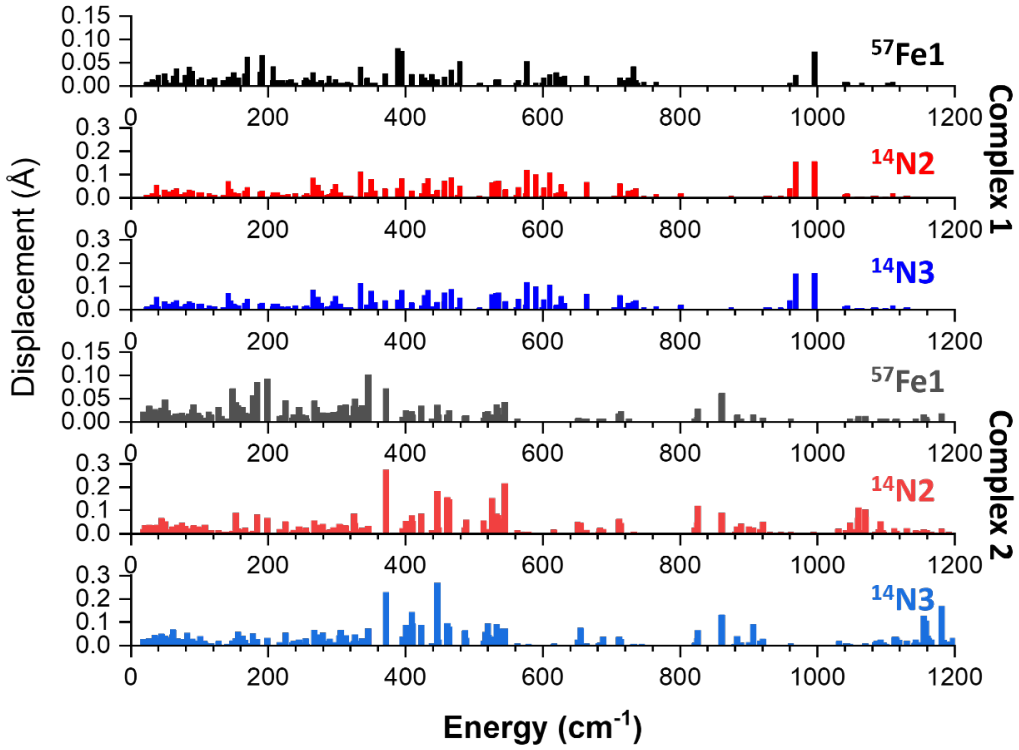

Figure S5. Calculated displacements of Fe and imido N atoms of each normal mode of vibration for complexes **1** and **2**.

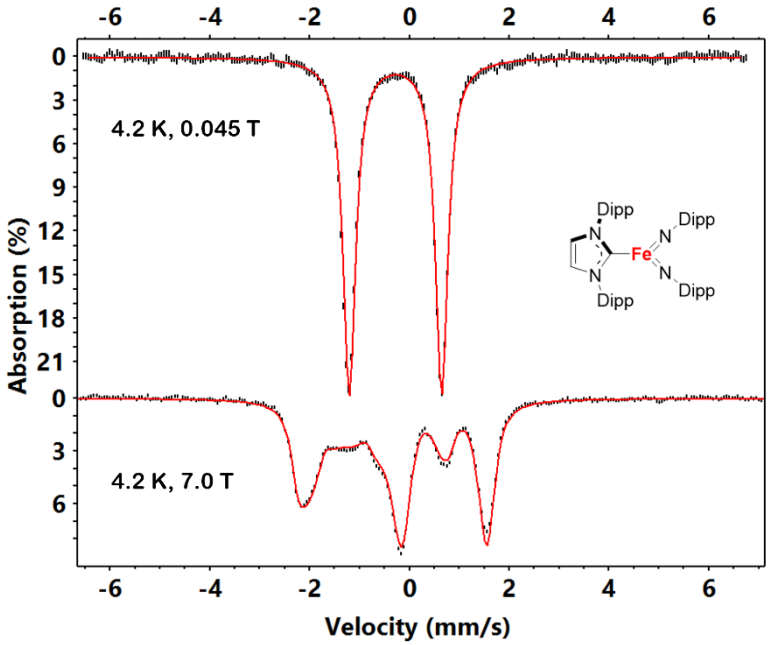

Figure S6. Mössbauer spectra of complex **1** measured at 4.2 K, 0.045 T (top) and 4.2 K, 7 T (bottom). The external field is parallel to the γ-radiation. Black vertical bars show experimental data with statistical errors. Red lines show the corresponding spectral simulations. Simulation parameters: $S = 0$, δ = -0.28 mm/s, ΔE_Q = -1.84 mm/s, η = 0.4.

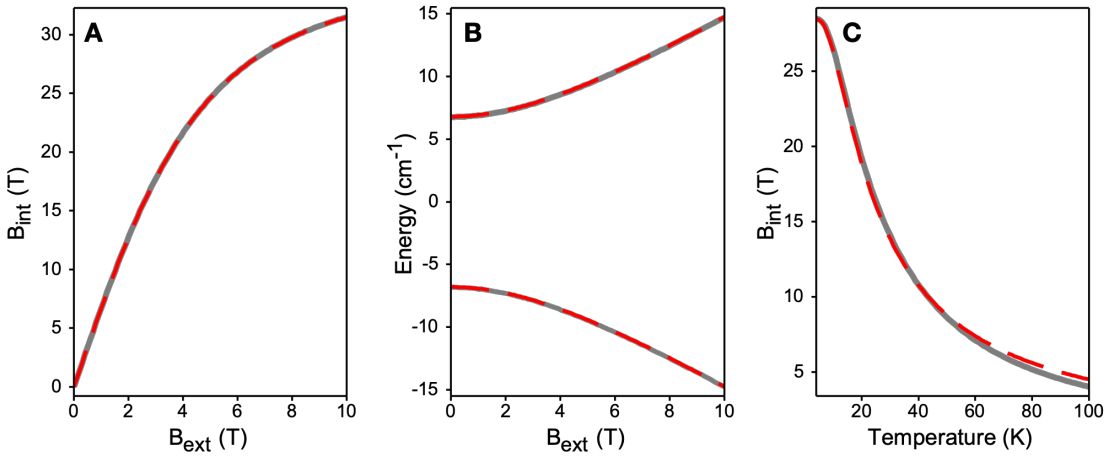

Figure S7. The comparison of the magnetization and the ground spin doublet sublevel energies derived from the canonical S = 1 spin Hamiltonian (grey solid lines) and the effective S = ½ spin Hamiltonian (red dash lines). (A) the internal field magnetization vs. the externally applied field of the ground spin sublevel; (B) the energy vs. the externally applied field of the ground spin doublet sublevels; (C) The internal field vs. temperature behavior with a constant externally applied field of 7 T.

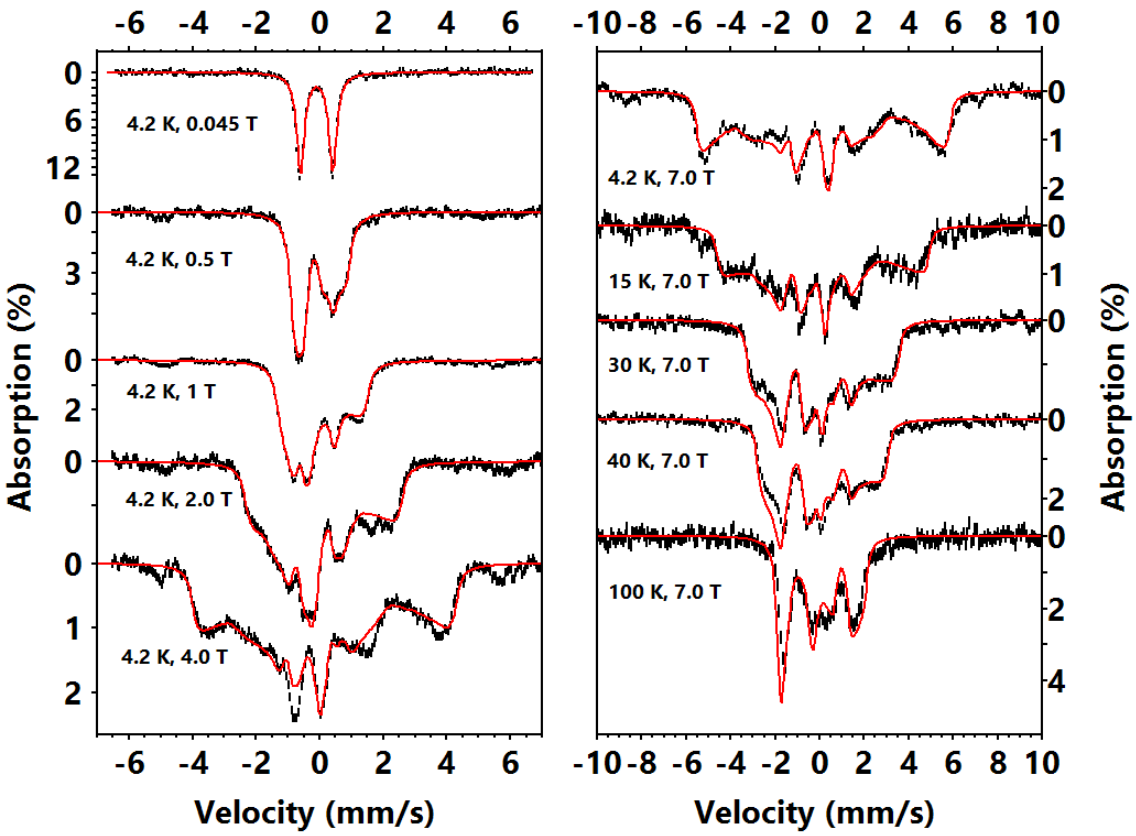

Figure S8. Mössbauer spectra of complex **2** measured under variant temperatures and external fields as indicated. The external field is parallel to the γ-radiation. Black vertical bars show experimental data with the statistical errors. Red lines show the corresponding simulations using the effective S = ½ spin Hamiltonian described in the main text and in the Mössbauer Simulation section in the SI.

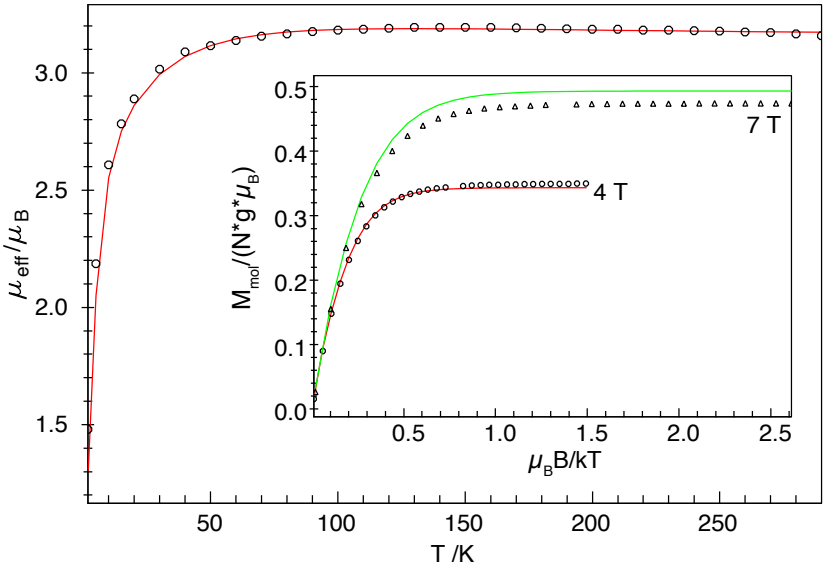

Figure S9. Temperature dependence of the magnetic moment, μ_{eff}, of a solid sample of complex **2** immobilized in eicosane recorded in a 1.0 T magnetic field and variable field and variable temperature dependence of the magnetization of complex **2** (inset). The solid lines represent best fits with $D = -79$ cm^{-1} (*fixed*), $E/D = 0.085$, $g_\perp = 1.83$, $g_\parallel = 2.80$, and TIP = 1188×10^{-6} emu.

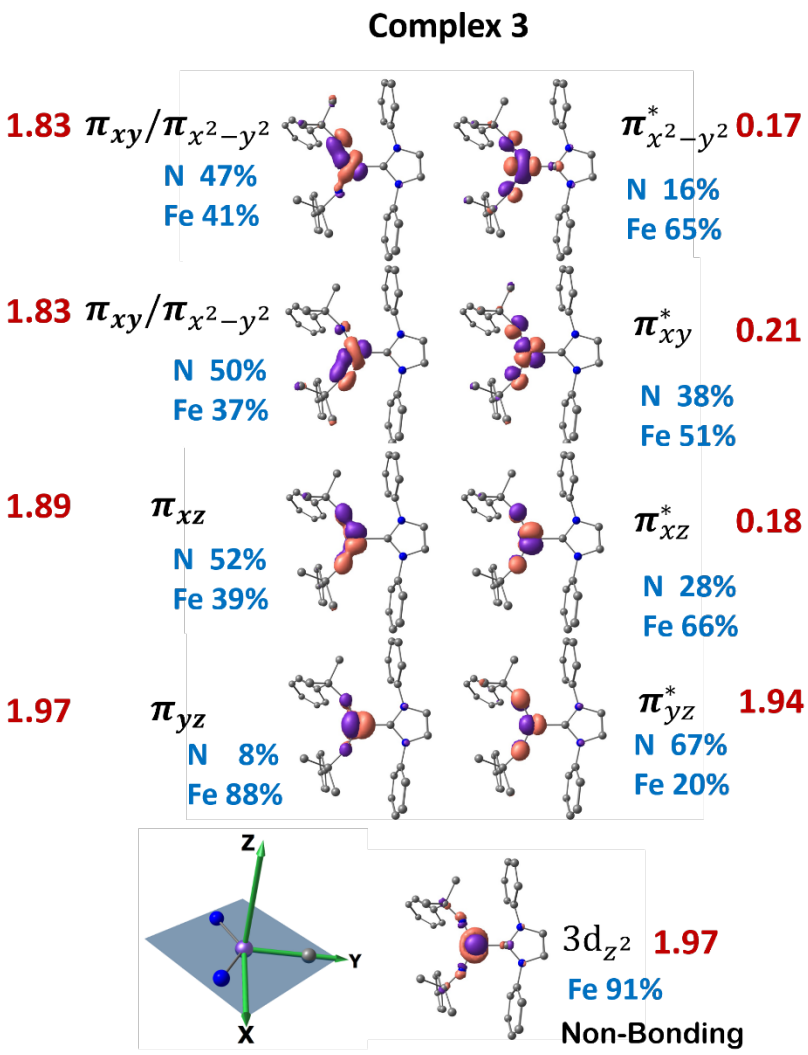

Figure S10. Natural orbitals and electronic configuration of calculation fragment of complex **3** obtained from a ground state CASSCF(9,12) calculation (Contour = 0.1). Labels show the molecular orbital symmetry notation (black), dominant atomic decomposition (blue) and occupation numbers (red). Inert shows the definition of cartesian frame for 3d orbital decomposition. All H atoms are omitted.

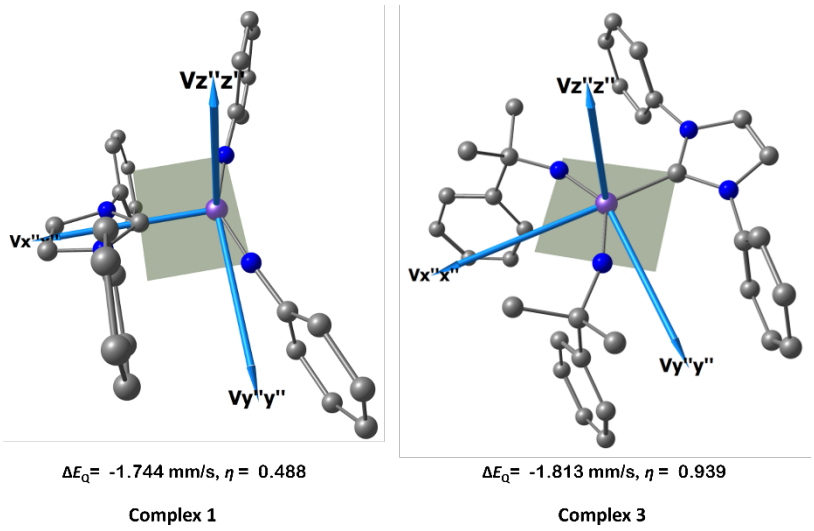

Figure S11. CASSCF/NEVPT2 calculated EFG tensor orientation of complex **1** (left) and complex **3** (right). All H atoms are omitted. The C-Fe(=NR)$_2$ planes are in grey.

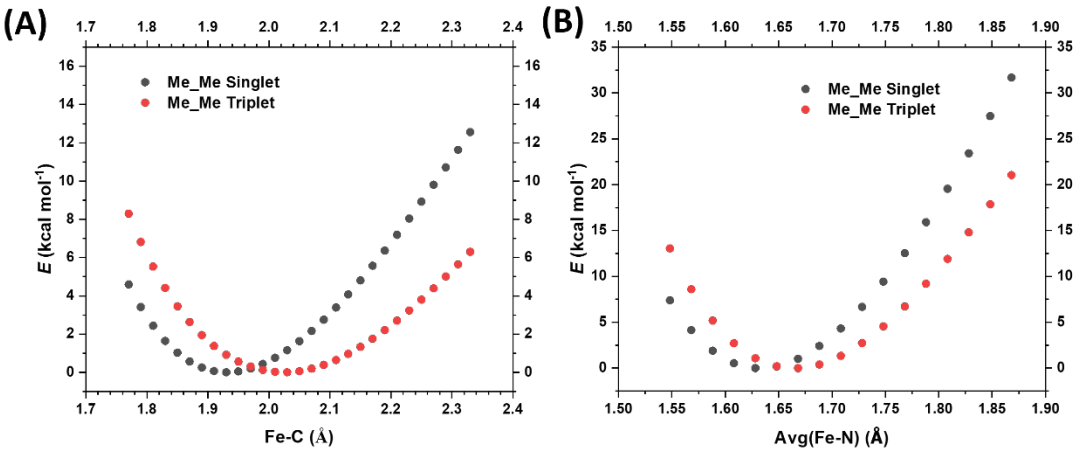

Figure S12. DFT scan of indicated candidate among selected geometric factors while freezing all the other condidates as described in the SI text: (A) Scan of Fe-C(NHC) bondlength, (B) Scan of Fe-N(imido) bondlength. For each data set, the energies are referred to the lowest energy among the set.

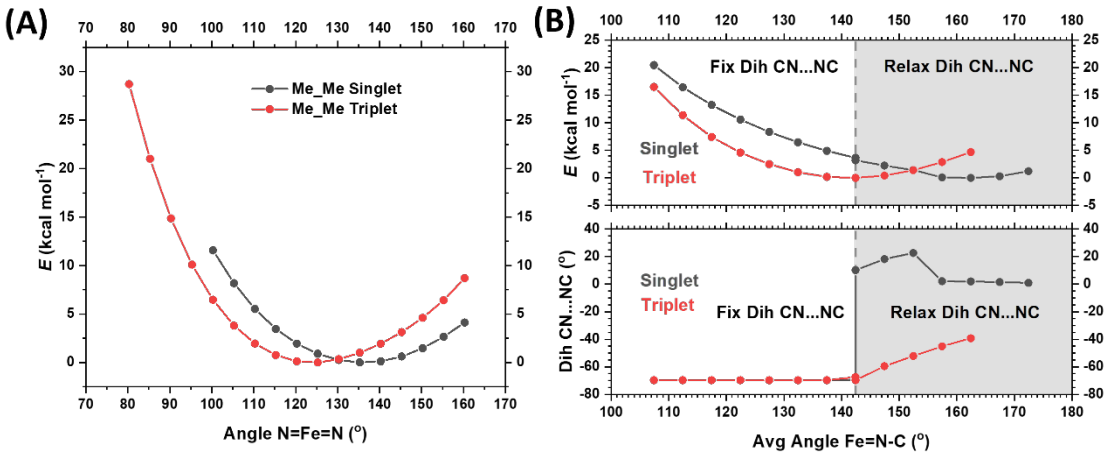

Figure S13. DFT scan of indicated candidate among selected geometric factors while freezing all the other condidates as described in the SI text: (A) Scan of N=F=N bond angle, (B) Scan of Fe=N-C bond angle: top panel is plots of Energy vs averaged Fe=N-C angle, while the bottom panel is plots of CN…NC dihedral angle vs averaged Fe=N-C angle. For each data set, the energies are referred to the lowest energy among the set. For the scan of Fe=N-C bond angle, the CN…NC dihedral angle has to be relaxed when the bond angles are larger than 144 degrees (See SI text for details).

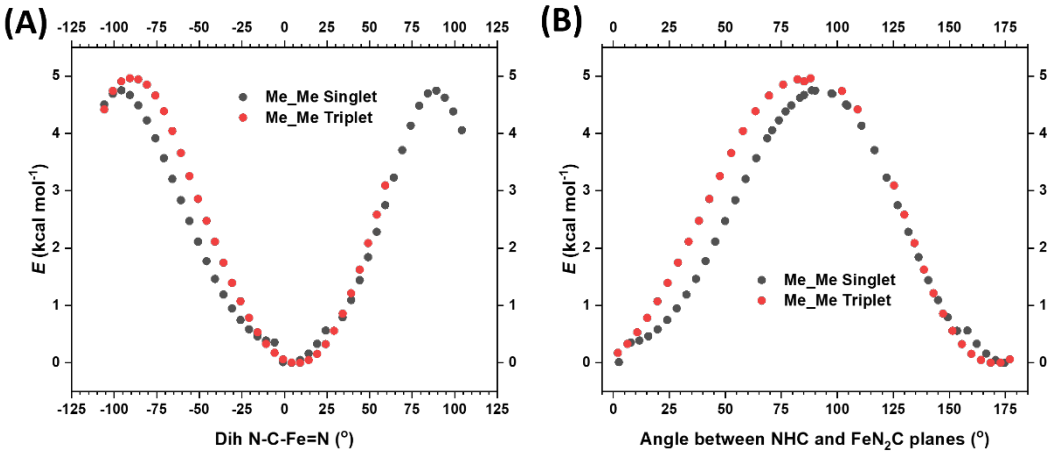

Figure S14. DFT scan of dihedral angle N-C-Fe=N while freezing all the other candidates as described in the SI text: (A) Plots of Energy vs dihedral angle N-C-Fe=N; (B) Plots of Energy vs the angle between NHC and C-Fe(=NR)$_2$ planes extracted from each stan step. For each data set, the energies are referred to the lowest energy among the set.

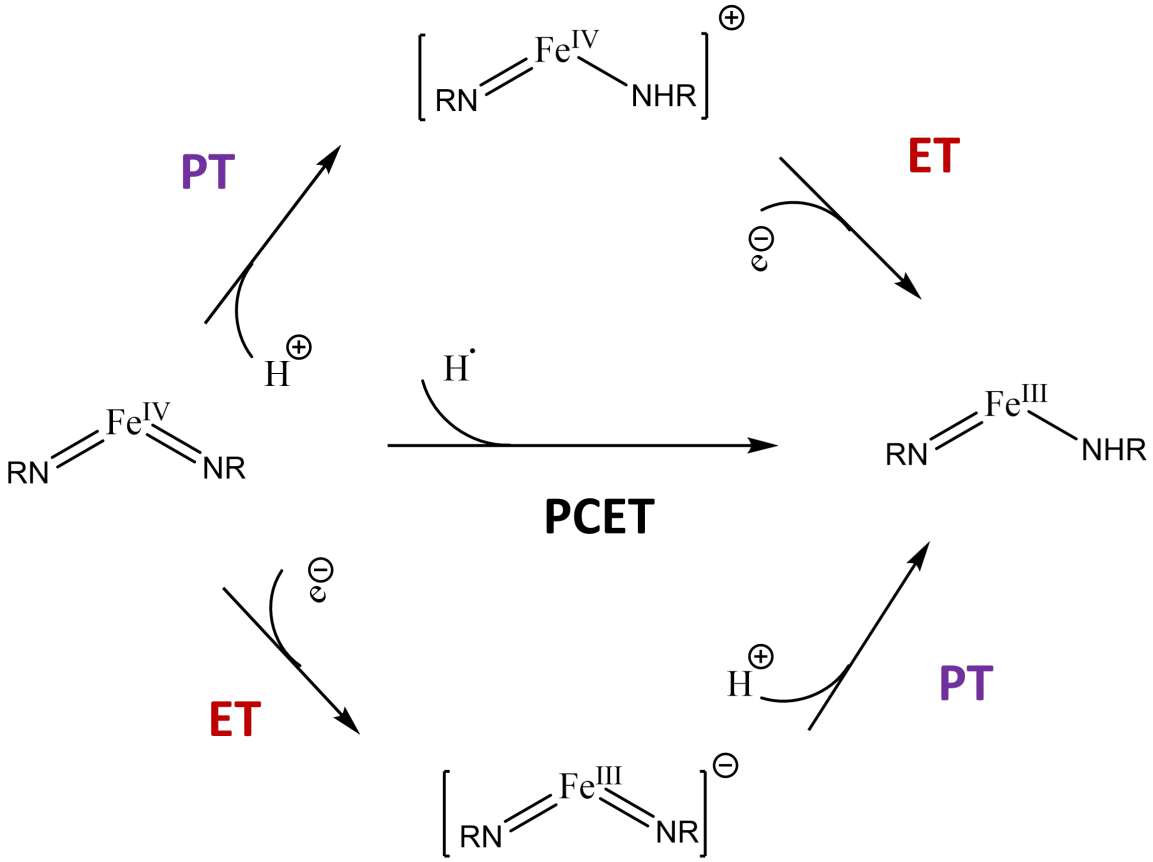

Figure S15.
The thermodynamic box scheme representing the concerted and the stepwise proton and electron transfer to connect an Fe(IV)=$(NR)_2$ species to a RN=Fe(III)-NHR species.

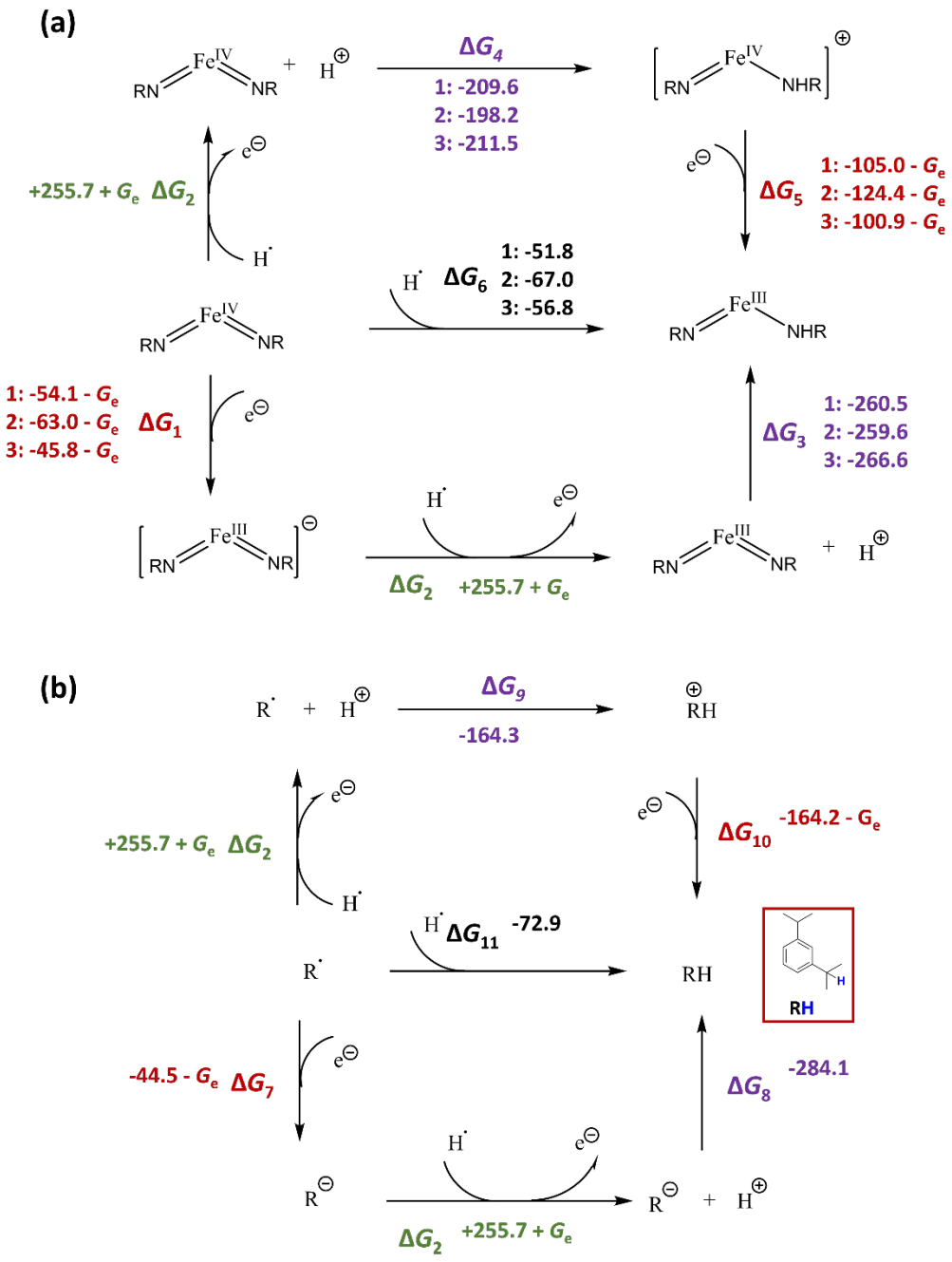

Figure S16. The thermodynamic box schemes representing (a) the bond dissociation free energy of a N-H bond in a RN=Fe(III)-NHR complex and (b) of the tertiary C-H bond in DippH (shown in the inset). The values shown are the free energy differences for a specific step in the unit of kcal/mol.

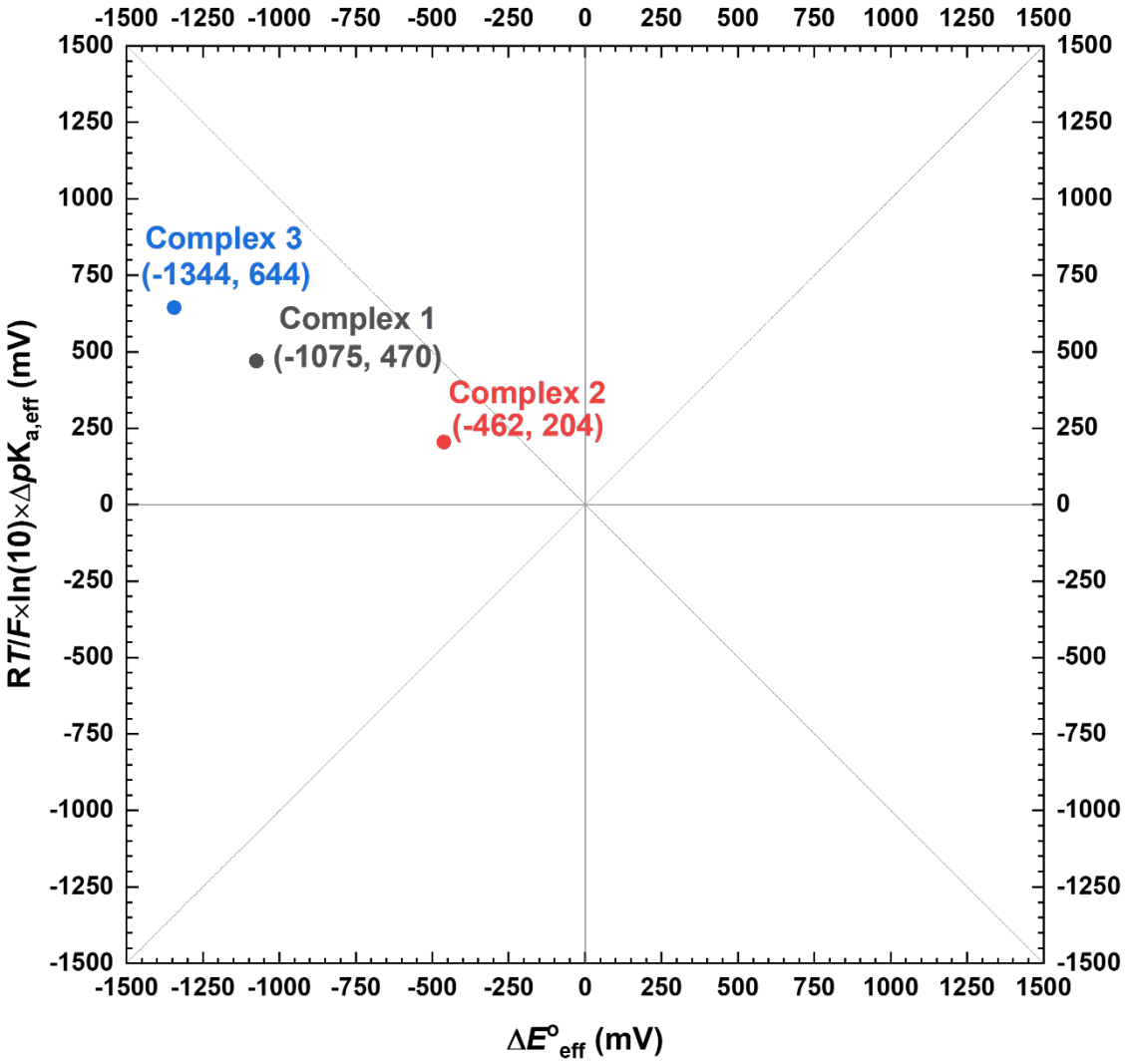

Figure S17. The correlation plot between ΔE^0_{eff} and RT/F×ln(10)×$\Delta pK_{a,eff}$ and their contributions to ΔE^0_H. The value is referring to abstracting the hydrogen atom from the one of the secondary carbons in 2,6-diisopropylbenzene (**Figure S16b** insert).

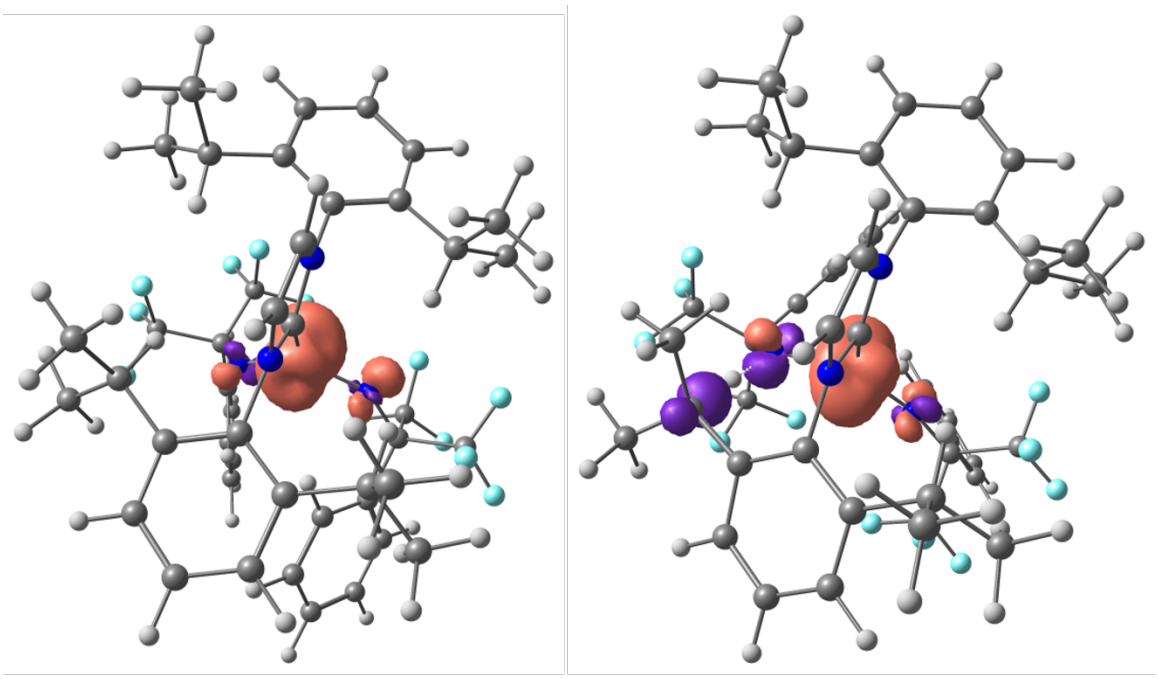

Figure S18. DFT calculated spin density plots of ground state (left) and transition state (right) of complex **2** based on the BP86/TZVP level of theory corrected with CPCM solvent model of benzene.

References

1. Zhang, H.; Ouyang, Z.; Liu, Y.; Zhang, Q.; Wang, L.; Deng, L., (Aminocarbene)(divinyltetramethyldisiloxane)iron(0) compounds: a class of low-coordinate iron(0) reagents. *Angew. Chem. Int. Ed. Engl.* **2014,** *53* (32), 8432-6.
2. Singh, A.; Singh, H.; Khurana, J. M., Recyclable zinc (II) ionic liquid catalyzed synthesis of azides by direct azidation of alcohols using trimethylsilylazide at room temperature. *Tetrahedron Letters* **2017,** *58* (25), 2498-2502.
3. Nesi, M.; Brasca, M. G.; Longo, A.; Moretti, W.; Panzeri, A., Generation of doubly trifluoromethylsubstituted carbocations: Synthesis of α,α-bis(trifluoromethyl)benzylamines. *Tetrahedron Letters* **1997,** *38* (27), 4881-4884.
4. Nguyen, Q.; Sun, K.; Driver, T. G., Rh_2(II)-catalyzed intramolecular aliphatic C-H bond amination reactions using aryl azides as the N-atom source. *J. Am. Chem. Soc.* **2012,** *134* (17), 7262-5.
5. Carlson, M. R.; Gray, D. L.; Richers, C. P.; Wang, W.; Zhao, P. H.; Rauchfuss, T. B.; Pelmenschikov, V.; Pham, C. C.; Gee, L. B.; Wang, H.; Cramer, S. P., Sterically Stabilized Terminal Hydride of a Diiron Dithiolate. *Inorg. Chem.* **2018,** *57* (4), 1988-2001.
6. Wang, L.; Hu, L.; Zhang, H.; Chen, H.; Deng, L., Three-coordinate iron(IV) bisimido complexes with aminocarbene ligation: synthesis, structure, and reactivity. *J. Am. Chem. Soc.* **2015,** *137* (44), 14196-207.
7. Liu, Q.; Long, L.; Ma, P.; Ma, Y.; Leng, X.; Xiao, J.; Chen, H.; Deng, L., Synthesis, structure, and C–H bond activation reaction of an iron(IV) terminal imido complex bearing trifluoromethyl groups. *Cell Reports Physical Science* **2021,** *2* (6).
8. Sheldrick, G. M., SHELXT - integrated space-group and crystal-structure determination. *Acta Crystallogr A Found Adv* **2015,** *71* (Pt 1), 3-8.
9. Sheldrick, G. M., Crystal structure refinement with SHELXL. *Acta Crystallogr. C* **2015,** *71* (Pt 1), 3-8.
10. Dolomanov, O. V.; Bourhis, L. J.; Gildea, R. J.; Howard, J. A. K.; Puschmann, H., OLEX2: a complete structure solution, refinement and analysis program. *J. Appl. Crystallogr.* **2009,** *42* (2), 339-341.
11. O'Connor, C. J., Magnetochemistry-Advances in Theory and Experimentation. In *Progress in Inorganic Chemistry*, 2007; pp 203-283.
12. Weast, R. C.; Astle, M. J., *CRC Handbook of Chemistry and Physics: A Ready-Reference Book of Chemical and Physical Data, 60th ed.* CRC Press Inc.: Boca Raton, Florida, 1979.
13. Nakagawa, I.; Shimanouchi, T., Infrared spectroscopic study on the co-ordination bond-II. *Spectrochimica Acta* **1962,** *18* (1), 101-113.
14. Zhao, J. Y.; Sturhahn, W., High-energy-resolution X-ray monochromator calibration using the detailed-balance principle. *J Synchrotron Radiat* **2012,** *19* (Pt 4), 602-8.
15. Sturhahn, W., CONUSS and PHOENIX: Evaluation of nuclear resonant scattering data. *Hyperfine Interactions* **2000,** *125* (1-4), 149-172.
16. Neese, F.; Wennmohs, F.; Becker, U.; Riplinger, C., The ORCA quantum chemistry program package. *J. Chem. Phys.* **2020,** *152* (22), 224108.
17. Weigend, F.; Ahlrichs, R., Balanced basis sets of split valence, triple zeta valence and quadruple zeta valence quality for H to Rn: Design and assessment of accuracy. *Phys. Chem. Chem. Phys.* **2005,** *7* (18), 3297-305.

18. Weigend, F., Accurate Coulomb-fitting basis sets for H to Rn. *Phys. Chem. Chem. Phys.* **2006,** *8* (9), 1057-65.
19. Kollmar, C.; Sivalingam, K.; Helmich-Paris, B.; Angeli, C.; Neese, F., A perturbation-based super-CI approach for the orbital optimization of a CASSCF wave function. *J. Comput. Chem.* **2019,** *40* (14), 1463-1470.
20. Frisch, M. J.; Trucks, G. W.; Schlegel, H. B.; Scuseria, G. E.; Robb, M. A.; Cheeseman, J. R.; Scalmani, G.; Barone, V.; Petersson, G. A.; Nakatsuji, H.; Li, X.; Caricato, M.; Marenich, A. V.; Bloino, J.; Janesko, B. G.; Gomperts, R.; Mennucci, B.; Hratchian, H. P.; Ortiz, J. V.; Izmaylov, A. F.; Sonnenberg, J. L.; Williams; Ding, F.; Lipparini, F.; Egidi, F.; Goings, J.; Peng, B.; Petrone, A.; Henderson, T.; Ranasinghe, D.; Zakrzewski, V. G.; Gao, J.; Rega, N.; Zheng, G.; Liang, W.; Hada, M.; Ehara, M.; Toyota, K.; Fukuda, R.; Hasegawa, J.; Ishida, M.; Nakajima, T.; Honda, Y.; Kitao, O.; Nakai, H.; Vreven, T.; Throssell, K.; Montgomery Jr., J. A.; Peralta, J. E.; Ogliaro, F.; Bearpark, M. J.; Heyd, J. J.; Brothers, E. N.; Kudin, K. N.; Staroverov, V. N.; Keith, T. A.; Kobayashi, R.; Normand, J.; Raghavachari, K.; Rendell, A. P.; Burant, J. C.; Iyengar, S. S.; Tomasi, J.; Cossi, M.; Millam, J. M.; Klene, M.; Adamo, C.; Cammi, R.; Ochterski, J. W.; Martin, R. L.; Morokuma, K.; Farkas, O.; Foresman, J. B.; Fox, D. J. *Gaussian 16 Rev. C.01*, Wallingford, CT, 2016.
21. Becke, A. D., Density-functional exchange-energy approximation with correct asymptotic behavior. *Phys Rev A Gen Phys* **1988,** *38* (6), 3098-3100.
22. Perdew, J. P., Density-functional approximation for the correlation energy of the inhomogeneous electron gas. *Phys Rev B Condens Matter* **1986,** *33* (12), 8822-8824.
23. Schäfer, A.; Horn, H.; Ahlrichs, R., Fully optimized contracted Gaussian basis sets for atoms Li to Kr. *J. Chem. Phys.* **1992,** *97* (4), 2571-2577.
24. Schäfer, A.; Huber, C.; Ahlrichs, R., Fully optimized contracted Gaussian basis sets of triple zeta valence quality for atoms Li to Kr. *J. Chem. Phys.* **1994,** *100* (8), 5829-5835.
25. Sage, J. T.; Paxson, C.; Wyllie, G. R. A.; Sturhahn, W.; Durbin, S. M.; Champion, P. M.; Alp, E. E.; Scheidt, W. R., Nuclear resonance vibrational spectroscopy of a protein active-site mimic. *J. Phys.: Condensed Matter* **2001,** *13* (34), 7707-7722.
26. Römelt, M.; Ye, S.; Neese, F., Clibration of modern density functional theory methods for the prediction of 57Fe Mössbauer isomer shifts: meta-GGA and double-hybride functionals. *Inorg. Chem.* **2009**, *48* (3), 784-785.
27. Grimme, S.; Antony, J.; Ehrlich, S.; Krieg, H., A consistent and accurate ab initio parametrization of density functional dispersion correction (DFT-D) for the 94 elements H-Pu. *J. Chem. Phys.* **2010,** *132* (15), 154104.
28. Barone, V.; Cossi, M., Quantum Calculation of Molecular Energies and Energy Gradients in Solution by a Conductor Solvent Model. *J. Phys. Chem. A* **1998,** *102* (11), 1995-2001.
29. Cossi, M.; Rega, N.; Scalmani, G.; Barone, V., Energies, structures, and electronic properties of molecules in solution with the C-PCM solvation model. *J. Comput. Chem.* **2003,** *24* (6), 669-681.
30. Tarrago, M.; Römelt, C.; Nehrkorn, J.; Schnegg, A.; Neese, F.; Bill, E.; Ye, S. Experimental and theoretical evidence for an unusual almost triply degenerate electronic ground state of ferrous tetraphenylporphyrin. *Inorg. Chem.* **2021**, *60* (7), 4966–4985.

31. Bim, D.; Maldonado-Dominguez, M.; Rulisek, L.; Srnec, M., Beyond the classical thermodynamic contributions to hydrogen atom abstraction reactivity. *Proc Natl Acad Sci U S A* **2018,** *115* (44), E10287-E10294.